UNIVERSITY OF BIRMINGHAM
University of Birmingham Research at Birmingham

Mesoscale modelling of selective laser melting

Panwisawas, Chinnapat; Qiu, Chunlei; Anderson, Magnus; Sovani, Yogesh; Turner, Richard; Attallah, Moataz; Brooks, Jeffery; Basoalto, Hector

DOI:
10.1016/j.commatsci.2016.10.011
10.1016/j.commatsci.2016.10.011

License:
Creative Commons: Attribution-NonCommercial-NoDerivs (CC BY-NC-ND)

Document Version
Peer reviewed version

Citation for published version (Harvard):
Panwisawas, C, Qiu, C, Anderson, M, Sovani, Y, Turner, R, Attallah, M, Brooks, J & Basoalto, H 2017, 'Mesoscale modelling of selective laser melting: Thermal fluid dynamics and microstructural evolution', *Computational Materials Science*, vol. 126, pp. 479-490. https://doi.org/10.1016/j.commatsci.2016.10.011, https://doi.org/10.1016/j.commatsci.2016.10.011

Link to publication on Research at Birmingham portal

Publisher Rights Statement:
Eligibility for repository: Checked on 24/10/2016

General rights
Unless a licence is specified above, all rights (including copyright and moral rights) in this document are retained by the authors and/or the copyright holders. The express permission of the copyright holder must be obtained for any use of this material other than for purposes permitted by law.

•Users may freely distribute the URL that is used to identify this publication.
•Users may download and/or print one copy of the publication from the University of Birmingham research portal for the purpose of private study or non-commercial research.
•User may use extracts from the document in line with the concept of 'fair dealing' under the Copyright, Designs and Patents Act 1988 (?)
•Users may not further distribute the material nor use it for the purposes of commercial gain.

Where a licence is displayed above, please note the terms and conditions of the licence govern your use of this document.

When citing, please reference the published version.

Take down policy
While the University of Birmingham exercises care and attention in making items available there are rare occasions when an item has been uploaded in error or has been deemed to be commercially or otherwise sensitive.

If you believe that this is the case for this document, please contact UBIRA@lists.bham.ac.uk providing details and we will remove access to the work immediately and investigate.

Download date: 18. Apr. 2024

Mesoscale modelling of selective laser melting: Thermal fluid dynamics and microstructural evolution

Chinnapat Panwisawas[1,*], Chunlei Qiu[1,2], Magnus J. Anderson[1], Yogesh Sovani[1], Richard P. Turner[1], Moataz M. Attallah[1], Jeffery W. Brooks[1], Hector C. Basoalto[1,*]

[1]School of Metallurgy and Materials, University of Birmingham, Birmingham B15 2TT, UK

[2]School of Engineering, Cardiff University, The Parade, Cardiff CF24 3AA, UK

Corresponding authors: c.panwisawas@bham.ac.uk, h.basoalto@bham.ac.uk

Abstract

In this paper, an integrated computational materials science approach for selective laser melting (SLM) at the mesoscale is presented. A particle dropping model was developed to simulate the representative powder-bed particle distribution of a measured titanium alloy powder. Thermal fluid flow and resulting microstructural evolution of a set of laser scanned single tracks with different powder layer thicknesses and scanning speeds during SLM were also studied using both computational and experimental approaches. The simulated powder particle distribution was found to be consistent with experimental measurement. The thermal fluid flow model predicts that single laser scanned tracks become increasingly irregular-shaped with increased powder layer thickness and increased laser scanning speed. These findings were reinforced by scanning electron microscopy analysis. The more dispersed dissipation of the localised heat for thicker powder layers is understood to cause increased melting and evaporation. This can lead to increased Marangoni force and recoil pressure which in turn destabilises the melt flow. The use of an argon atmosphere speeds up the solidification process when compared with air but does not affect the morphology of single tracks significantly. The predicted microstructure was consistent with the electron backscattered diffraction data. The microstructure-based modelling methodology considering

the representative powder size distribution provides a good predictive capability for the laser-powder interaction behaviour, surface structure and porosity development.

Keywords: *Multi-scale materials modelling, Selective laser melting, Thermal fluid dynamics, Microstructure prediction, Ti-6Al-4V*

1. Introduction

Additive manufacturing (AM) is a novel processing route of increasing interest to a wide number of industries and applications, including those for safety-critical aerospace and gas turbine components. Metallic components, especially parts in jet engines, can be both fabricated and repaired using the AM technique; however this requires stringent quality control measures to assure part integrity, as the process can be susceptible to defects such as; sub-surface porosity [1], poor surface finish [2], and undesirable microstructure [3]. It is also likely to produce some level of residual stress and distortion [3]. Computational modelling therefore can provide an important tool to better understand the physical phenomena, thus acting as a precursor to tailored experimental procedure. Modelling of additive manufacturing processes within both industry and academia has proven a very new area of interest. Owing to the similarities between additive manufacture and more traditional fusion-welding techniques, Panwisawas et al. [4] have recently shown that laser powder-bed fusion AM have adopted similar computational techniques from the more advanced laser fusion welding models. Broadly, modelling work in to AM to date has either focused upon small-scale interactions between heat and powder particles on evaporation simulation [5], on powder absorption [6] or on the effect of process parameters [7]. Although, the mechanical properties of the fabricated component have been experimentally reported both in nickel alloys [8] and in titanium alloys [9]; the comprehensive understanding on melt flow behavior and the microstructural development is still lacking.

Research on experiments of SLM has been either concentrated on characterising densification, microstructure and property [10] or using X-ray diffraction to better understand cracking bahaviour [11]. Recently, Zhou et al. [12] have reported more advanced 3D-imaging of SLM defects by synchrotron radiation micro-CT, whereas Tan et al. [13] have intensively studied on the microstructure and mechanical behaviour produced from electron beam melting (EBM) using transmission electron microscopy. Parimi et al. [3] have reported the microstructure analysis of direct laser deposition samples affected to distortion and Parimi et al. [14] provided insight into the effect of process parameters to microstructure and texture. None of those has numerially rationalised the effect of melt flow charcteristic to microstructure evolution. The interaction of the laser heat source with the powder particles (and of the powder particles interaction with each other), is a complex process upon which those processes are reliant. However, Panwisawas et al. [1] have proposed a model to simulate this complex phenomenon via thermal fluid flow calculation, in order to predict and rationalise the evolution of the metallic/gaseous interface which was backed up experimentally by Qiu et al. [2]. Recently, Khairallah et al. [15] have rationalised physics of complex melt flow via modelling of energy absortion and Megahed et al. [16] have taken into account the different chemical concentration of materials to simulate the thermal fluid flow during both SLM and DLD processes. This underlying mechanism can be used as a physics-based tool to predict the porosity and surface structure once the representative powder distribution is physically simulated.

To better understand the melt flow mechanics of the powder particles within SLM, it is essential to envisage a representative statistical distribution of the powder particles using a randomly packed powder bed configuration using a 2D lattice Boltzmann as demonstrated [17] or a “particle-raining” model proposed by Zhou et al. [18], with some modifications, whereby the powder particles are dropped in to place within a packed configuration. It is

understood that (i) the size distribution of powder particles, (ii) packing density and (iii) deposited layer thickness all provoke distinct powder packing configurations and hence statistical characteristics. This allows for a probabilistic function of densification or porosity density as a function of energy density, layer thickness, or scanning speed to be constructed. Experimentally measured Ti-6Al-4V powder size distributions reported by Qiu et al. [9] have been used as a sample space for picking up a randomly selected particle, and dropped one-by-one into the deposition layer configuration, until this build layer is filled to the desired thickness. After pre-spreading of powder feedstock, the melt flow behaviour is predicted using thermal fluid dynamics calculation to qualify and quantify the sub-surface structure and porosity as a function of laser scanning speed, laser power, powder layer thickness and the powder particle configuration.

The structural properties of the SLM-produced component are known to be dependent upon the processing-induced microstructure as mentioned previously, which in turn is influenced by initial particle size distribution and thermal fluid history. Understanding the SLM microstructure evolution with the consideration of laser-powder behaviour allows for improved understanding of the structural properties and component integrity. To the best of the authors' knowledge, a microstructure-based approach for the determination of optimised SLM process parameters, considering the causal-and-effect relationships between solid-liquid interactions of the powder particles and the SLM process route, is rarely reported in literature. In this work, a mesoscale modelling approach (considering from first principles the simulation of the heat source and powder particle interactions to allow for prediction of microstructure) has been employed to the simulation of SLM using Ti-6Al-4V alloy. The model focuses on predicting micro-scale defects and simulating processing-induced microstructure using the representative powder size distribution. Powder sweeping, processing-induced porosity, surface morphology and as-fabricated microstructure, i.e. grain

morphology and texture, are predicted with the proposed modelling approach, and all backed up with relevant experimentation.

2. Modelling Approach

The integrated computational materials engineering (ICME) framework is implemented to model the SLM process in Ti-6Al-4V alloys. The multi-scale approach is summarised in Figure 1. In this paper, we focus on the mesoscale modelling. Use has been made of the measured powder size distribution to randomly pick up particles and arrange these particles in place to replicate the sweeping process during SLM. The laser scanning is then applied via modelling of the interaction between heat source and powder particles. The single track scanning is then performed to derive the temperature history and molten zone morphology, which is used to predict the SLM-process induced grain microstructure. Thereafter, the linkage between micromodel and macroscale simulation by communicating the physics at mesoscale is being reported by Sovani et al. [19].

2.1 Powder size distribution model

To investigate the melting behaviour of powder particles during SLM it is necessary to numerically generate similar powder particle arrangements for simulation. Our previous work, Qiu et al. [9], suggested that the as-received Ti-6Al-4V powder particle size falls into the range of 20 – 50μm in diameter based on laser scattering measurement. A probability density function (PDF) (Gaussian fit) is then used to simulate the probability or frequency of each particle size and by integrating PDF for different powder particle sizes, a cumulative distribution function has been developed to simulate the measured powder particle size distribution. The measured and fitted cumulative distribution functions are compared in Figure 2(a).

To simulate the position and arrangement of powder particles with a representative size distribution in a layer, a method, proposed by Zhou et al. (2009), which involves dropping particles following a trajectory based on the geometry of the objects encountered has been adopted and modified. This approach ignores the motion of obstacles encountered by the falling particles and the trajectory of a particle is determined based on the number of obstacles being encountered. Several potential obstacles and corresponding trajectories of a falling particle are illustrated in Figures 2(b) to 2(e). The dropping sequence of powder particles was determined using a face-centred cubic (FCC) lattice, which ensures that the particles were dropped layer-by-layer. The exact location of the *x*-*y* drop coordinate was offset by a random amount in a random direction. The distance was a maximum of 20% of the lattice parameter used to generate the lattice.

The algorithm detected any obstacle encountered by the falling particle along its trajectory. A new trajectory was determined based upon the number of obstacles encountered, as illustrated in Figures 2(b), (c), (d) and (e). A particle can only come to rest if it encounters three stable obstacles or falls on the floor. The particles were dropped parallel to the *z* axis with periodic boundary conditions being applied along the *x* and *y* axis. The powder dropping model provides a calculation domain through which the desired layer thicknesses can be achieved and the thermal fluid flow calculation can be performed; see Figure 3(a).

2.2 Melt flow kinetics

To further investigate the thermal fluid flow characteristics giving rise to surface structure, porosity development and microstructure simulation, a computational fluid dynamics (CFD) calculation using the C++ open source CFD toolbox so-called Open Field Operation and Manipulation (OpenFOAM®) has been developed to model the interaction between the laser heat source and the randomly distributed Ti-6Al-4V powder materials, which is illustrated in

Figure 3(b). In the model, all interfacial phenomena, including surface tension (capillary force), Marangoni's flow (thermo-capillary force), recoil pressure, drag force due to solid/liquid transition via Darcy's term, and buoyancy force, present within the SLM process have been included in simulation. The energy dissipation in the mushy zone during melting, and heat loss due to evaporation, conduction, convection and radiation have also been taken into account in this work. However, a layer of computational complexity is required for energy reflections of the laser beam (this would require a coupling of the electromagnetics equations), this has been excluded in this work. Instead, volumetric laser heat source representing energy reflection has been used. The coupling of the Navier-Stokes equation, energy conservation, continuity equation and volume-of-fluid equation is solved using a single set of equations to describe metallic and gaseous phases in order to simulate the evolution of the liquid/gas interface. The summation of metallic α_1 and gaseous phases α_2 is always unity, i.e. $\alpha_1 + \alpha_2 = 1$, in every fluid element. In this study, the gaseous phase is assumed to be air atmosphere, unless specified otherwise. Additionally, a weight function of any parameter x is used to smear out the effect of metallic and gaseous phases, defined as, $\bar{x} = x_1\alpha_1 + x_2\alpha_2$.

For this CFD calculation, we assume that the material is incompressible, i.e. the continuity condition satisfies

$$\boldsymbol{\nabla} \cdot \boldsymbol{u} = 0 \tag{1}$$

where, $\boldsymbol{u}$ is flow velocity. The volume-of-fluid equation used to predict the evolution of the liquid/gas interface, is expressed as

$$\frac{\partial \alpha_1}{\partial t} + \boldsymbol{\nabla} \cdot (\alpha_1 \boldsymbol{u}) = -\frac{\dot{m}_V}{\rho_2} \tag{2}$$

where t is time, and the sink term in the right hand side (RHS) describes the loss of metallic phase due to evaporation when the evaporation temperature T_V is reached. In this work, ρ_2 is

referred to the density of metal vapour which is not different from atmospheric gas phase as chemical species is not distinguished here. The mass evaporation rate $\dot{m}_V$ (per unit volume) is defined as

$$\dot{m}_V = p_V \sqrt{\frac{m}{2\pi k_B T}} \tag{3}$$

and the recoil pressure p_V is phenomenologically described by

$$p_V(T) = p_0 \exp\left\{\frac{\Delta H_V}{R}\left(\frac{1}{T_V} - \frac{1}{T}\right)\right\}, \tag{4}$$

where p_0, ΔH_V and R are atmospheric pressure, enthalpy change due to evaporation and universal gas constant, respectively. The evaporation model (Equations (3)) followed the Hetrz-Knudsen model, assuming that there was no back condensation of vapour molecules. The role of the gas phase on evaporation is not excluded from this work. The phenomelogical model for recoil pressure has followed Courtois et al.[20] to estimate the momemtum flux through the liquid/vapour interface.

As reported previously by [1,2], the beginning of interaction between heat source and the materials during SLM predicts the kinetics of the melt pool. All interfacial forces present during the SLM process have been inserted into the conservation of momentum or Navier-Stokes equation, which is in the form of

$$\frac{\partial \bar{\rho}\boldsymbol{u}}{\partial t} + \boldsymbol{\nabla}\cdot(\bar{\rho}\,\boldsymbol{u}\otimes\boldsymbol{u}) = -\boldsymbol{\nabla}p + \boldsymbol{\nabla}\cdot\bar{\bar{T}} + \bar{\rho}\,g\hat{\boldsymbol{e}}_{\boldsymbol{z}}\,\beta\left(T - T_{ref}\right) - K_C\left(\frac{(1-f_L)^2}{f_L^3 + C_K}\right)\boldsymbol{u} + \left[\sigma\kappa\hat{\boldsymbol{n}} + \frac{d\sigma}{dT}\left(\boldsymbol{\nabla}T - \hat{\boldsymbol{n}}(\hat{\boldsymbol{n}}\cdot\boldsymbol{\nabla}T)\right) + \hat{\boldsymbol{n}}\left(p_V\mathbb{I}\cdot\hat{\boldsymbol{n}}\right)\right]|\boldsymbol{\nabla}\alpha_1|\,\frac{2\bar{\rho}}{(\rho_1+\rho_2)} \tag{5}$$

Eq. (5) implies the rate of change of fluid momentum on the left hand side (LHS) is driven by all interfacial forces on the RHS. Divergence of stresses is comprised of hydrostatic pressure, p, and viscous deviatoric stress tensor, $\bar{\bar{T}}$, expressed as

$$\bar{\bar{T}} = 2\bar{\mu}\left[\left(\frac{1}{2}\boldsymbol{\nabla}\boldsymbol{u} + \frac{1}{2}(\boldsymbol{\nabla}\boldsymbol{u})^T\right) - \frac{1}{3}(\boldsymbol{\nabla}\cdot\boldsymbol{u})\mathbb{I}\right]. \tag{6}$$

Here, $\bar{\rho}$ is the density, $\bar{\mu}$ is viscosity and $\mathbb{I}$ is the identity matrix. The third terms on RHS of Eq. (5), to the first approximation, Boussinesq approximation, $\bar{\rho}\, g\hat{\boldsymbol{e}}_{\boldsymbol{z}}\beta\left(T - T_{ref}\right)$, are used to describe buoyancy force caused by density differences due to thermal expansion, where g and $\hat{\boldsymbol{e}}_{\boldsymbol{z}}$ are the magnitude and unit normal of gravitational force, β is thermal expansion coefficient, T is temperature field and T_{ref} is the reference temperature, equal to 300K in this case. It is noted that the Boussinesq approximation used for this SLM processing route is subject to high temperatures, therefore the initial timestep to ensure good boundedness of the problem must be very small, of the order of a nano-second. Darcy's term, $-K_C\left(\frac{(1-f_L)^2}{f_L^3+C_K}\right)\boldsymbol{u}$, which is energy dissipation or sink (damping) terms in the mushy zone is modelled in this work by making use of the Carman-Kozeny equation – an enthalpy method for phase chages – as described by Voller et al [21] and Rösler and Brüggemann [22], where K_C, f_L and C_K are permeability coefficient, fraction of liquid metal and constant, respectively. There are three surface force terms considered here:

(i) $\sigma\kappa\hat{\boldsymbol{n}}$ - surface tension term (capillary force), with surface tension σ, acting on surface curve κ at the unit normal $\hat{\boldsymbol{n}}$, after Brackbill et al.[23] and Sun and Beckermann [24].

(ii) $\frac{d\sigma}{dT}\left(\boldsymbol{\nabla}T - \hat{\boldsymbol{n}}(\hat{\boldsymbol{n}}\cdot\boldsymbol{\nabla}T)\right)$ - Marangoni force (thermo-capillary force) proposed by Scriven and Sternling [25] and Ytrehus and Østomo [26], taking into account the effect of temperature gradient on the liquid/gas interface, More details can be found in [27].

(iii) $\hat{\boldsymbol{n}}(p_V\mathbb{I}\cdot\hat{\boldsymbol{n}})$ - recoil pressure when evaporation occurs.

All surface forces have been applied only at the interface indicated by the interface term $|\boldsymbol{\nabla}\alpha_1|$ and the sharp surface force term $\frac{2\bar{\rho}}{(\rho_1+\rho_2)}$ is used to smear out between hard (metallic) and soft (gaseous) phases. The conservation of total energy is written as

$$\frac{\partial \bar{\rho}\,\bar{C}_p T}{\partial t} + \nabla\cdot\left(\bar{\rho}\,\boldsymbol{u}\bar{C}_p T\right) = -\frac{\partial \bar{\rho}\,\Delta H_f}{\partial t} - \nabla\cdot\left(\bar{\rho}\,\boldsymbol{u}\Delta H_f\right) + \nabla\cdot\left(\bar{k}\nabla T\right)$$
$$-\left[\left(h_c\left(T - T_{ref}\right) + \sigma_s\epsilon\left(T^4 - T_{ref}^4\right) + Q_V\right)|\nabla\alpha_1| - Q_T\right]\frac{2\bar{C}_p\bar{\rho}}{\left(\bar{C}_{p1}\rho_1 + \bar{C}_{p2}\rho_2\right)} \quad (7)$$

The thermal energy is balanced between heat input due to the heat source term Q_T (per unit volume), proposed by Xu et al. [28],

$$Q_T(r,z) = \frac{\zeta\eta q_{\text{laser}}}{\pi(1-e^{-3})(E+F)}\left(\frac{1-\chi}{z_e - z_i}z + \frac{\chi z_e - z_i}{z_e - z_i}\right)\exp\left(-\frac{3r^2}{r_0^2(z)}\right)$$

-- the heat source term is a function of power distribution factor ζ, effective absorption factor η, total laser power q_{laser}, beam radius z_e -- and heat loss due to conduction, $\nabla\cdot\left(\bar{k}\nabla T\right)$, convection, $h_c\left(T - T_{ref}\right)$, radiation, $\sigma_s\epsilon\left(T^4 - T_{ref}^4\right)$ and evaporation, $Q_V \sim \dot{m}_V \Delta H_V$. Here, $\bar{C}_p$ is specific heat for the mixture, $\bar{k}$ is thermal conductivity of the mixture, ΔH_f is the enthalpy change due to fusion, h_c is heat transfer coefficient, σ_s is Stefan-Boltzmann constant, ϵ is emissivity, and E, F, z_i, χ and r_0 are model parameters according to Xu et al. [28]. Note that Jin et al. [29] has proposed a multiple energy reflection model in laser fusion and 3D energy reflection [30], which can be physically captured in Geiger et al. [31] and in [20] using the couple of electomagnetic equation with thermal fluid flow ones. It is believed that the heat source model compared with the aboved mentions is able to capture the energy absorption as numerically confirmd in [32]. By solving the set of equations (1), (2), (5) and (7), the evolution of melt kinetics and liquid/gas interface change can be analysed and rationalised. A detailed model description is being published [32] and model parameters were adopted from Li et al. [33] on high temperature thermal physical property, and Rai et al. [34] and Rai et al. [35] on thermal fluid flow parameters. They are tabulated in Table 1 and Table 2. The CFD model has been applied to the generated powder particle distribution with an calculation domain of 250μm × 1000μm × 250μm, containing 500000 elements with the constant hexagonal mesh size of 5μm, and a laser heat source of 400 W with a scanning

speed of 2400 and 4000 mm/s to simulate the processing condition. The modelling results are compared with the relevant experimentation.

2.3 Evolution of grain microstructure

The solidification that involves grain nucleation and growth during SLM process was simulated using a three-dimensional cellular automaton – finite element (CAFE) code using the approach proposed by Kurz et al. [36] and Rappaz and Gandin [37]. Gandin and Rappaz [38] has later developed the code for 2D simulation of solidification in casting process and Gandin et al. [39] applied to solidification and grain growth in 3D casting situation. The CAFÉ module within the ESI Group ProCAST software [37-39] was developed as a commercial piece of code, and has been utilised in this work. As far as the computational time and resources are concerned, the CAFÉ method can allow numerous simulations to run, allowing the user to obtain a stochastic data-set within a reasonable timescale, which will be beneficial for a material design purpose. The molten single track and temperature history along the scanning were exported from the OpenFOAM CFD model described in Section 2.2 and used to define the solidification regions and dynamics, temperature boundary conditions and the moving laser heat source and temperature profile. In the CAFE model, the cellular automation grid was re-meshed with a hexagonal mesh size of 2 μm along the molten scanning track. A continuous nucleation distribution, $\frac{dn}{d(\Delta T_c)}$, is used to describe the increase of grain density, dn, induced by the increase in the undercooling, $d(\Delta T_c)$. The total density of grains at a specific (ΔT_c), is defined by

$$n(\Delta T_c) = \int_0^{\Delta T_c} \frac{dn}{d(\Delta T')} [1 - f_s(T')] d(\Delta T') \quad (5)$$

and

$$\frac{dn}{d(\Delta T_c)} = \frac{n_{\max.}}{\Delta T_{c_0} \sqrt{2\pi}} \exp\left(-\frac{\Delta T_c - \overline{\Delta T_c}}{\sqrt{2}\Delta T_{c_0}}\right)^2 \quad (6)$$

where f_s is the volume fraction of solid already formed. With the aid of the KGT model by Kurz et al. [36], growth kinetics of a dendritic tip, described by the dendritic tip velocity, $v(\Delta T_c)$, related to its undercooling can be expressed in Equations (5)-(8) of Rappaz and Gandin [37] and Gandin and Rappaz [38], which can be approximated to be

$$v(\Delta T_c) = a_2 \Delta T_c^{\,2} + a_3 \Delta T_c^{\,3} \quad (7)$$

The parameters a_2 and a_3 have been calculated using a Ti-6Al-4V thermodynamics database, as tabulated in Table 3. In a CAFÉ model, the finite element (FE) calculation of the thermal field has been coupled with the CA grain growth model. The CA dendritic growth algorithm was dependent upon the thermal gradient and isotherm velocity which in turn gave the undercooling temperature and had been solved in the thermal FE scheme. The thermal field from the tetrahedral FE mesh was then interpolated to be the grain growth hexahedral CA mesh to obtain dendritic growth, provided that a homogeneous nucleation condition was assumed. Grain morphology and texture can be predicted thereafter.

The evolution of SLM-induced microstructure can be rationalised and predicted in terms of grain morphology and texture. The grain growth modelling is compared with the scanning electron micrograph (SEM) and electron back-scattered diffraction (EBSD) results.

3. Experimental

The material used in this study was gas atomised Ti-6Al-4V powder supplied by TLS Technik (Germany) in the size range of 20-50μm. The powder particle size distribution is shown in Fig. 3(c). The single track scanning trials were performed on powder layers with different thicknesses ranging from 20μm up to 100μm at 400W and 2400mm/s or on a single layer of powder with thickness of 20μm but with different laser scanning speeds from 2000mm/s up to 4000mm/s at 400W, in order to study the influence of powder layer

thickness and laser scanning speed on the geometrical and microstructural development of single tracks during SLM. Prior to single track trials, cubic samples 10×10×3mm were built at 400W and 2400mm/s (which gave rise to smooth top/uppermost surfaces, as followed (Qiu et al., 2015) and then powder layers with different thicknesses were spread over the top surfaces of these samples for different single track laser scans. This is to avoid the inhomogeneous powder spreading and distribution in the first several layers over a normal build plate and also to get close to the actual building condition. The laser scanned tracks were then studied by SEM in terms of morphology and width and also cross sectioned, polished and etched in an etchant containing 50 ml distilled water, 25 ml HNO_3 and 5 ml HF for SEM and ESBD study.

4. Results

4.1 Powder particle size distribution

Figure 3(a) shows the simulated powder particle distribution for different layer thicknesses including 20-40, 60, 80, 100 and 120 μm, obtained by using the current particle dropping model. It is clear that the simulated powder particle distribution has a good agreement with the observed particle distribution, as shown in Figures 3(c) and 3(d). This suggests that the current particle dropping model is effective in simulating the three-dimensional particle arrangement, which establishes a good foundation for the advanced modelling development such as the thermal fluid flow calculation that involves complex laser-powder interaction.

4.2 Single track morphology, porosity formation and melt flow behaviour

To understand the interaction between laser beam and powder layers and the resulting melt flow behaviour during SLM, single track scanning over powder layers has been performed and simulated by CFD modelling. Figure 4 shows the comparison of the morphology of single scanned tracks obtained through CFD modelling and SEM examination. Obviously,

the simulated single track morphologies are fairly consistent with experimental observations. The denudation has been observed experimentally, which might originate from the rearrangement of solid particles by the surface tension of the wetting melt. This results consistent with [40]. The laser scanning over a thin layer such as the 20μm thick powder layer gives rise to a generally smooth and continuous track (Figure 4(a) and 5(a)) whereas increased layer thickness tends to generate discontinuous and rugged tracks. These discontinuities are consistent with those observed on the uppermost surfaces of SLM processed bulk Ti-6Al-4V samples [2]. Features such as cave-like pores that occurred due to unstable melt flow could also be observed occasionally (see Figures 4 and 5). The increasingly rugged tracks and increased discontinuities at increased layer thicknesses are believed to be responsible for the increased uppermost surface roughness and irregularity observed on the bulk samples that have been demonstrated in our previous work [2]. Moreover, it is noted that with increased powder layer thickness, the heat dissipation after laser scanning has become increasingly dispersive and widespread through the neighbouring powder particles around the laser scanned paths as seen clearly in Figures 4(b), 4(c) and 4(d). This is suspected to cause more melting of powder particles and thus more metal evaporation, which could lead to increased Marangoni force and recoil pressure that would destabilise melt pool and flow, consistent with the high speed photography results in [2] showing the high velocity magnitude at thick layers.

Figures 4(e) and 4(f) shows the influence of atmosphere and laser scanning speed on laser scanned single track development (in comparison with Figure 4(a)). It seems that the use of argon atmosphere (as shown in Figure 4(e)) through altering the thermal fluid property discipate more thermal energy in the melt flow as compared with air atmosphere and thus speeds up solidification and cooling. However, the morphology of single track remains almost unaffected. This result suggests that the surface forces are far more important in

affecting melt flow behaviour and resultant surface structure than thermal history during SLM. The former was found to have caused significant influence on the stability of melt flow during SLM. The increased laser scanning speed, however, was found to lead to more irregular-shaped laser scanned track as evidenced by Figures 4(f) and 5(f) in comparison with Figure 4(a). This is consistent with previous work by [2] where increased laser scanning speed was found to cause increasingly irregular-shaped uppermost surface structure. Additionally, splashing of small particles has been found when the 4000mm/s laser scanning was used.

Figure 6 illustrates the comparison between experimental porosity measurement and modelling results. It indicates that the porosity prediction has been accurately captured when the representative powder distribution is used. For a given layer powder thickness, five instances of particle distribution have been generated to provide some statistical information for which porosity volume fraction can be predicted. After single track scanning, molten zone has been taken to calculate the densification using an in-house code scanning the region where no solid metal was found. The code scanned through the whole molten track, filtered out the solid cells and calculated the volume where the cluster of gas cells assembled. The error bars in Figure 6 indicate the variation of porosity fraction over five sampling instances and the solid dots show the average value. Moreover, the single-mode powder particle distribution of the average size of 50μm shows some discrepancy away from the experimental observation, particularly at 100μm layer thickness. It suggests that distributed powder modelling accurately captures laser-powder interaction behaviour, surface structure and porosity development as compared with that developed based on single-mode powder particle distribution.

4.3 Microstructure development during SLM process

A novel numerical technique to link the thermal fluid dynamics calculation and SLM-processed grain microstructure prediction is presented here. The internal field variable has been written to track the region that is melted. In this way, the single track can be traced and acts as a solidification region where dynamic temperature boundary condition can be derived from CFD model and assigned to replicate the moving laser heat source. Figures 7(a) and 7(b) show the molten zone of 20μm and 100μm layer thicknesses, respectively. The rapid solidification from liquid to solid after SLM has then been simulated using Cellular Automata algorithm. Figures 7(c) and 7(d) shows the predicted fraction solid and misorientation (θ) – defined as an angles misaligning from the perfectly preferential growth direction of the material – at 20μm and 100μm layer thicknesses, respectively. The evolution of grain solidification during SLM proceeds such a way that the grains generally grow normal to the solidification front (i.e., the melt-solid interface), giving rise to the development of columnar grains within the solidified solid. Also, the current modelling further confirms that SLM is a very rapid solidification process as the solidification front rate could reach 10 m/s.

Cross sections of some of the weld beads have been further studied by using SEM and EBSD. Figure 8 shows the SEM observation results on the cross sections of two weld beads fabricated with 20μm and 100μm layer thicknesses together with the modelling results on grain structure development. It is obvious that columnar prior β grains have been developed during SLM of single tracks, which is generally consistent with the modelling results (Figure 7). The bottom region of the simulated tracks tend to show more random and equiaxed grains (as shown in Figure 8(a)) probably because bulk substrate is assumed in the modelling which assumes identical heat loss in all directions through the substrate and as a result the bottom region of the melt pool that is in contact with substrate would tend to develop grains from all directions. In contrast, in the current experiment single tracks were made upon an actual build which would allow for epitaxial growth of columnar grains that are already within the build.

However, the grains in the upper region of the predicted weld beads are much more columnar, closer to the situation within the real build. Moreover, the experimental observation suggests that weld beads are significantly dominated by martensitic needles which could pass through several grains in a slant angle, consistent with previous [9]. The layer thickness, however, does not significantly affect the microstructure.

EBSD results, as shown in Figure 9, further confirm that α′ phase has dominated in the weld beads. Due to very limited β phase present, confirmed by [9], and that α′ needles have passed through several grains, the prior β grains are not revealed in the EBSD micrographs. According to the EBSD results, there seem to be strong α′ microtexture along $\{10\bar{1}0\}$ crystallographic orientation. The β texture is not as obvious, probably due to its very limited amount. It is consistent with the prediction of as-fabricated texture in Figure 10 showing that the random β texture predicted for two weld beads fabricated with 20μm and 100μm layer thicknesses. Misorientation maps of 20μm track and 100μm track is calculated to be normal distribution with the average misorientaion around 32°, and grain size distribution of 20μm track and 100μm track is approximately 6μm and 13μm in size.

5. Discussion

The use of distributed powder particles from the experiment provides a better representation for SLM powder-bed process, compared with the single-mode powder distribution. It suggests that the laser-materials interaction boundary is very important, contributing to surface morphology. The laser-materials interaction boundary depends upon the powder particle size, particle morphology, particle distribution, packing density and powder layer thickness, all of which contribute into stochastic behaviour of surface structure and the resulting sub-surface porosity. As such, the development of modelling based on the current representative powder particle size distribution is significant and will give rise to better

prediction in laser-material interaction, surface structure and porosity development. The 20μm powder layer thickness, filtering the particle with the below averaged size to sit on the substrate, demonstrates good surface finish as the energy density is high enough for the materials to fully melt. More importantly, the powder arrangement is rather compact, consistent with the fully-packed single-mode arrangement of the 50 μm spherical particles giving rise to the similar low level of porosity (see Figure 6). The variation in the laser-materials interaction boundary comes when the layer thickness increased. The spatial dispersion due to the different particles size lead to non-homogeneity in packing density, e.g. larger particles might obstruct the smaller ones to fall in between as a result leaving behind gaps between them. The imperfection of the particle shape itself, such as smaller satellite particles agglomerated to the larger particles, may lead to different surface morphology and sub-surface features.

The current modelling developed upon the representative powder particle distribution further suggests that the stochastic features of the powder particles are significantly contributed into the surface structure and the resulting sub-surface voids/pores. The proof-of-concept experiments has been designed to validate rigorously the single track scanning which is hardly performed using a flat substrate as the friction between the flat substrate and the first powder layer particles is very low and is not representative to the fabrication process. The results also demonstrated that the surface morphology of the scanning track with different powder layer thicknesses matches very well with experiments. For the 20μm layer thickness, the surface structure is very smooth as the melt flow behaviour is driven by relatively high energy density. Whereas, the higher layer thickness combined with the packing density due to the distributed feature spreading into the scanning domain affects the energy density received by the powder and also particles splashing can be expected as discussed in [2]. The spatter of small particles is observed in both modelling and experiments. It will leave behind the even

surface structure and sub-surface voids and/or cave-like pores. The effect seems to be pronounced when increasing the powder layer thickness or laser scanning speed as a result of the unstable flow at thicker layer thicknesses or higher laser scanning speed. The use of argon atmosphere was found to alter the thermal conductivity and resulting thermal field but does not change the surface morphology of the builds significantly as compared with the use of air in the modelling. The results suggest that further investigation of multi-phase modelling of SLM is anticipated.

To simulate the microstructural development during SLM, a novel approach has been developed to link up the fluid flow and grain growth model. The highly dynamic process of SLM has been simulated via exporting the molten zone and associated dynamics temperature boundaries from CFD results. With assumptions of homogeneous nucleation on the substrate and nucleation volume of the molten track, the prediction of the SLM-processed microstructures could be made using a phenomenological law of Gaussian distribution of nucleation and growth. This work has highlighted that the empirical law is dependent upon the available data which was taken from the casting situation, to the first approximation. Microstructural predictions here will be strongly reliant upon the temperature gradient which dictates the directional growth of the grains. The high thermal gradient of SLM enables the columnar grain structure to be grown following the melt pool boundary, considered as the solidification for the process. The time taken to solidify for 200μm length is up to 15ms, further confirming that the solidification process after SLM is a rapid process. Within such a short timescale, it is very difficult for nuclei to be developed within melt pool and as a result the development of equiaxed grains has been very much suppressed during SLM. The substrate and the grains within the previous layers could act as natural nuclei for grain development in the next layer and the thermal difference between the melt pool and the substrate promotes epitaxial growth of columnar grains. The prediction of grain morphology

and texture still needs some improvement; nevertheless, qualitative information from the predictions appears to be reliable. SEM micrographs reveal further that columnar grains are dominant as observed along the cross-sectional views of 20μm and 100μm powder layer thicknesses, which is consistent with the modelling results. It suggests that solidification front and thermal profile are important to process control.

Summary and Conclusions

A mesoscopic model of the AM process has been developed and validated. The following specific conclusion can be drawn from this work.

(1) Powder size distribution has been accurately modelled using the measured size distribution. A powder sweeping model for the representative SLM powder bed process was successfully developed

(2) Thermal fluid flow results are consistent with experimental observation on single scanned tracks, both suggesting that with increased powder layer thickness and increased laser scanning speed, the tracks become increasingly irregular-shaped.

(3) Solidification microstructure within SLM process can be influenced by the powder layer thickness and also by altering the surrounding atmosphere from air to argon, leading to change in thermal and solidification behaviour of the melt pools but not significantly affect the morphology of the solidified tracks.

(4) A linkage between thermal fluid flow and microstructure evolution has been established which gives rise to good prediction in grain structure development during SLM. The predicted as-fabricated microstructure is dependent upon localised solidification conditions and the thermal profile.

Acknowledgements

C.P, M.J.A, Y.S, R.P.T, H.C.B, J.W.B thank the support by the Centre for Advanced Simulation and Modelling collaborative project between Rolls-Royce plc, Manufacturing Technology Centre and the University of Birmingham and the support by the European Regional Development Fund. C.Q and M.M.A acknowledge the support by AMAZE project (Additive Manufacturing Aiming towards Zero Waste and Efficient Production of High-Tech Metal Products) which is funded by the 7th Framework Programme of the European Commission.

References

[1] C. Panwisawas, C.L. Qiu, Y. Sovani, J.W. Brooks, M.M. Attallah, H.C. Basoalto, On the role of thermal fluid dynamics into the evolution of porosity during selective laser melting, Scr. Mater. 105 (2015) 14 – 17 .

[2] C.L. Qiu, C. Panwisawas, R.M. Ward, H.C. Basoalto, J.W. Brooks, M.M. Attallah, On the role of melt flow into the surface structure and porosity development during selective laser melting, Acta Mater. 96 (2015) 72 – 79.

[3] L.L. Parimi, M.M. Attallah, J.C. Gebelin, R.C. Reed, Direct laser fabrication of Inconel-718: Effects on microstructure and distortion, Superalloy2012, ed. by E.S. Huron et al. (Warrendale, PA : TMS, 2012), pp. 511-519.

[4] C. Panwisawas, Y. Sovani, R.P. Turner, H. Jasak, H. Nilsson, I. Choquet, J.W. Brooks, H.C. Basoalto, Physics-based keyhole modelling of laser fusion welding in titanium alloys: Keyhole dynamics, thermal fluid flow, and porosity formation, Submitted.

[5] F. Verhaeghe, T. Craeghs, J. Heulens, L. Pandelaers, A pragmatic model for selective laser melting with evaporation, Acta Mater. 57 (2009) 6006 – 6012.

[6] C.D. Boley, S.A. Khairallah, A.M. Rubenchik, Modelling of powder absorption in additive manufacturing. Optical Society of Merica CLEO, 2014.

[7] S.A. Khairallah, A. Anderson, Mesoscopic simulation model of selective laser melting of stainless steel powder. J. Mater. Proc. Technol. 214 (2014) 2627–2636.

[8] K.N. Amato, S.M. Gaytan, L.E. Murr, E. Martinez, P.W. Shindo, J. Hernandez, S. Collins, F. Medina, Microstructures and mechanical behaviour of Inconel 718 fabricated by selective laser melting, Acta Mater. 60 (2012) 2229 – 2239.

[9] C.L. Qiu, N. J. E. Adkins, M. M.Attallah, Microstructure and tensile properties of selectively laser-melted and of HIPed laser-melted Ti–6Al–4V, Mater. Sci. Eng.: A578 (2013) 230 – 239.

[10] Q. Jia, D. Gu, Selective laser melting additive manufacturing of Inconel 718 superalloy parts: Densification, microstructure and properties. J. Alloys Comp. 585 (2014) 713 – 721.

[11] L.N. Carter, C. Martin, P.J. Withers, M.M. Attallah, The influence of the laser scan strategy on grain structure and cracking behaviour in SLM powder-bed fabricated nickel superalloy. J. Alloys Comp. 615 (2014) 338 – 347.

[12] X. Zhou, D. Wang, X. Liu, D. Zhang, S. Qu, J. Ma, G. London, Z. Shen, W. Liu, 3D-imaging of selective laser melting defects in a Co-Cr-Mo alloy by synchrotron radiation micro-CT, Acta Mater. 98 (2015) 1 – 16.

[13] X. Tan. Y. Kok. Y.J. Tan, M. Descoins, D. Mangelinck, S.B. Tor, K.F. Leong, C.K. Chua, Graded microstructures and mechanical properties of additive manufactured Ti-6Al-4V via electron beam melting, Acta Mater. 97 (2015) 1 – 16.

[14] L.L. Parimi, Ravi G.A., D. Clark, M.M. Attallah, Microstructural and texture development in direct laser fabricated IN718, Mater. Char. 89 (2014) 102 – 111.

[15] S.A. Khairallah, A.T. Anderson, A. Rubenchik, W.E. King, Laser powder-bed fusion additive manufacturing: Physics of complex melt flow and formation mechanisms of pores, spatter, and denudation zones, Acta Mater. 108 (2016) 36 – 45.

[16] M. Megahed, H.W. Mindt, N. N'Dri, H. Duan, O. Desmaison, Metal additive-manufacturing process and residual stress modelling, Integrating Materials and Manufacturing Innovation 5:4 (2016) 1 – 33.

[17] C. Körner, E. Attar, P. Heinl, Mesoscopic simulation of selective beam melting processes. J. Mater. Proc. Technol. 211 (2011) 978 – 987.

[18] J. Zhou, Y. Zhang, J.K. Chen, Numerical simulation of random packing of spherical particles for powder-based additive manufacturing. J. Manuf. Sci. Eng. 131 (2009) 031004.

[19] Y. Sovani, C. Panwisawas, R.P. Turner, J.W. Brooks, H.C. Basoalto, Property switching element approach to modelling of additive layer manufacturing, in preparation.

[20] M. Courtois, M. Carin, P.L. Masson, S. Gaied, M. Balabane, A new approach to compute multi-reflection of laser beam in a keyhole for heat transfer and fluid flow modelling in laser welding, J. Phys. D: Appl. Phys. 46 (2013) 505305(14pp).

[21] V.R. Voller, M. Cross, N.C. Markatos, An enthalpy method for convection/diffusion phase change, Int. J. Num. Meth. Eng. 24 (1987) 271-284.

[22] F. Rösler, D. Brüggemann, Shell-and-tube type latent heat thermal energy storage: numerical analysis and comparison with experiments, Heat Mass Transfer 47 (2011) 1027–1033.

[23] J.U. Brackbill, D.B. Kothe, C. Zemach, A continuum method for modelling surface tension, J. Comp. Phys. 100 (1992) 335–354.

[24] Y. Sun, C. Beckermann, Diffuse interface modelling of two-phase flows based on averaging mass and momentum equations**,** Physica D 198 (2004) 281–308.

[25] L.E. Scriven, C.V. Sternling, The Marangoni effects, Nature 187 (1960) 186–188.

[26] T. Ytrehus, S. Østomo, Kinetic theory approach to interphase processes, Int. J. Multiphase Flow 22 (1996) 133–155.

[27] H. Ki, P.S. Mohanty, J. Mazamder, Modelling of high-density laser-material interaction using fast level set method, J. Phys. D: Appl. Phys. 34 (2001) 364–372.

[28] G.X. Xu, C.S. Wu, G.L. Qin, X.Y. Wang, S.Y. Lin, Adaptive volumetric heat source models for laser beam and laser + pulsed GMAW hybrid welding process, Int. J. Adv. Manuf. Technol. 57 (2011) 245–255.

[29] X. Jin, L. Li, Y. Zhang, A study on Fresnel absorption and reflections in the keyhole in deep penetration laser welding, J. Phys. D: Appl. Phys. 35 (2002) 2304–2310.

[30] X. Jin, P. Berger, T. Graf, Multiple reflections and Fresnel absorption in an actual 3D keyhole during deep penetration laser welding, J. Phys. D: Appl. Phys. 39 (2006) 4703–4712.

[31] M. Geiger, K.-H. Leitz, H. Kock, A. Otto, A 3D transient model of keyhole and melt pool dynamics in laser beam welding applied to the joining of zinc coated sheets, Prod. Eng. Res. Devel. 3(2009) 127–136.

[32] C. Panwisawas, Y. Sovani, R.P. Turner, H. Jasak, H. Nilsson, I. Choquet, J.W. Brooks, H.C. Basoalto, Physics-based keyhole modelling of laser fusion welding in titanium alloys: Keyhole dynamics, thermal fluid flow, and porosity formation. In preparation.

[33] J.Z. Li, W.L. Johnson, W.K. Rhim, Thermal expansion of liquid Ti-6Al-4V measured by electrostatic levitation, Appl. Phys. Lett. 89 (2006) 111913(2pp).

[34] R. Rai, J.W. Elmer, T.A. Palmer, T. DebRoy, Heat transfer and fluid flow during keyhole mode laser welding of tantalum, Ti-6Al-4V, 304L stainless steel and vanadium, J. Phys. D: Appl. Phys. 40 (2007) 5753–5766.

[35] R. Rai, P. Burgardt, J.O. Mileewski, T.J. Lienert and T. DebRoy, Heat transfer and fluid flow during electron beam welding of 21Cr-6Ni-9Mn steel and Ti-6Al-4V alloy, J. Phys. D: Appl. Phys. 42 (2009) 025503(12pp).

[36] W. Kurz, B. Giovanola, R. Trivedi, Theory of microstructural development during rapid solidification, Acta Metall. 34 (1986) 823–830.

[37] M. Rappaz, Ch.-A. Gandin, Probabilistic modelling of microstructure formation in solidification processes, Acta Metall. Mater. 41 (1993) 345–360.

[38] Ch.-A. Gandin, M. Rappaz, A coupled finite element-cellular automaton model for the prediction of dendritic grain structures in solidification processes, Acta Metall. Mater. 42 (1994) 2233–2246.

[39] Ch.-A. Gandin, J.-L. Desbiolles, M. Rappaz, Ph. Thevoz, A three-dimensional cellular automaton-finite element model for the prediction of solidification grain structures, Metall. Mater. Trans.: A30 (1999) 3153 – 3165.

[40] M.J. Matthews, G. Guss, S.A. Khairallah, A.M. Rubenchik, P.J. Depond, W.E. King, Denudation of metal powder layers in laser powder bed fusion processes, Acta Mater. 114 (2016) 33-42.

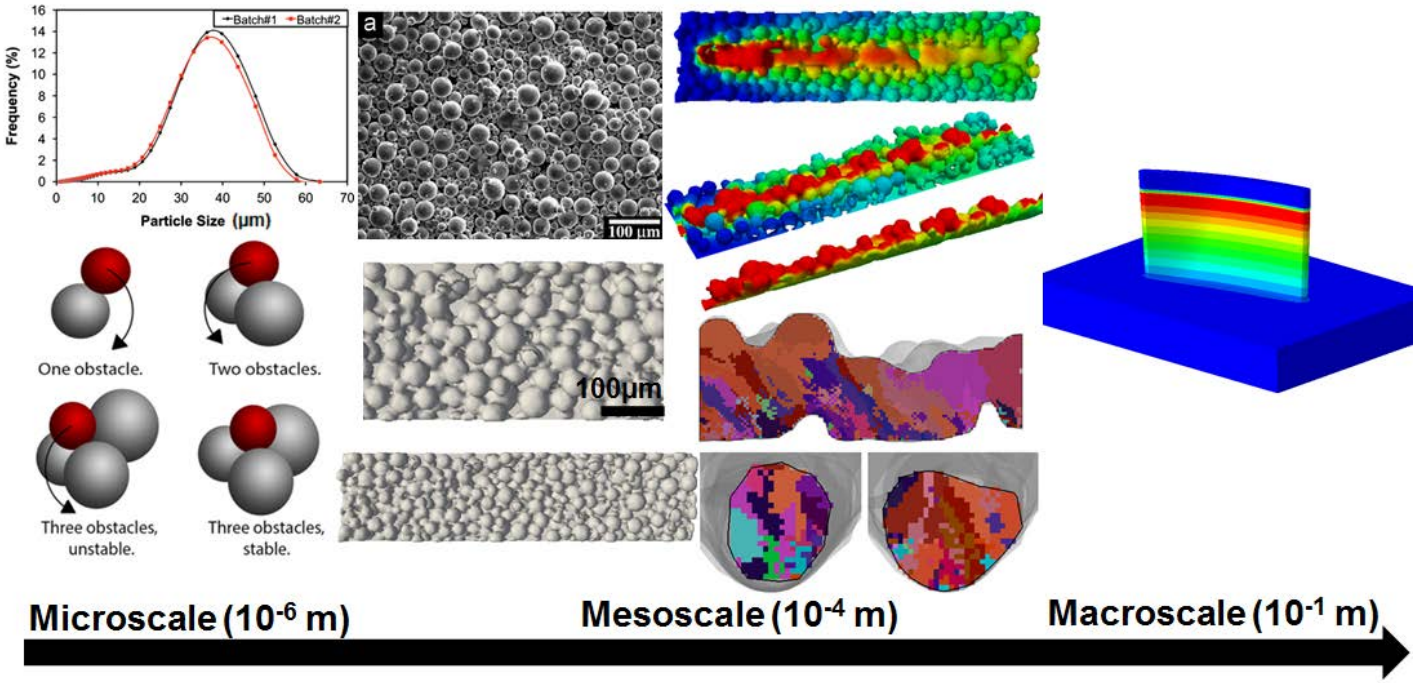

Figure 1: A multi-scale materials approach to modelling of selective laser melting in titanium alloys.

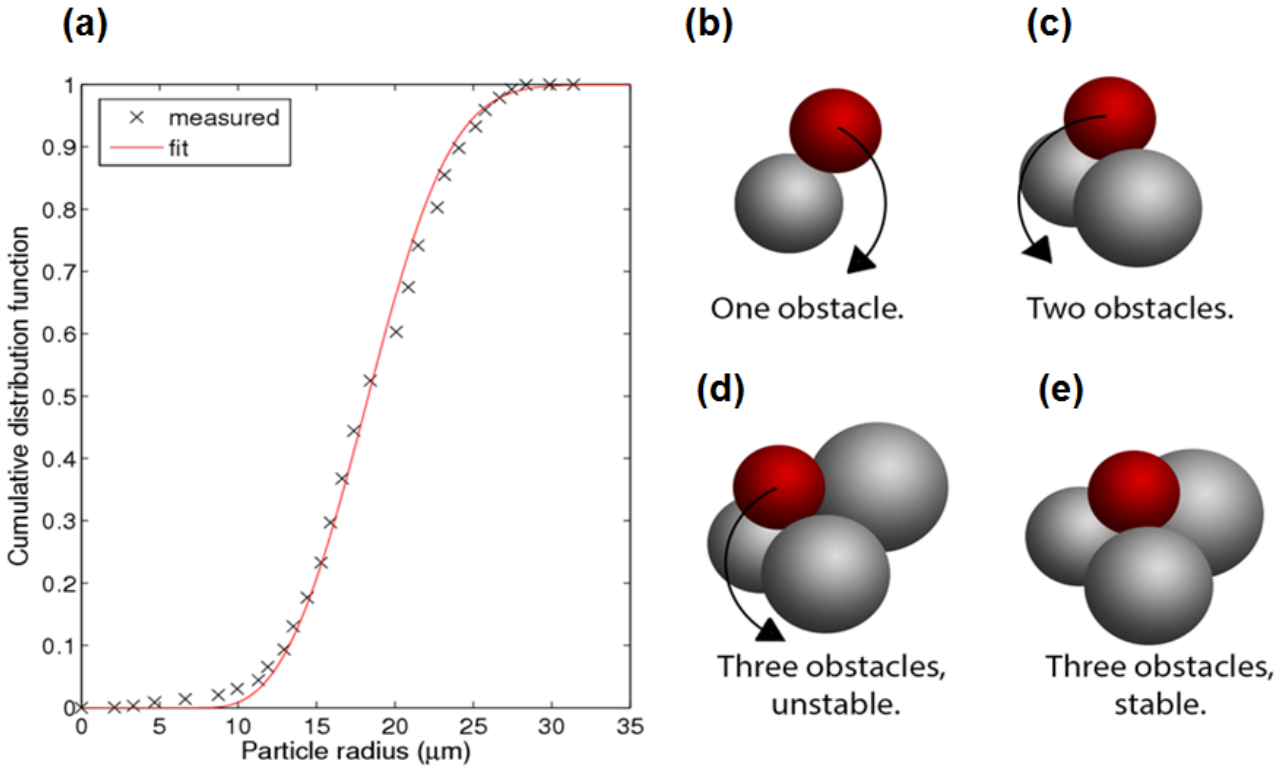

Figure 2: (a) cumulative distribution function used for powder particle sweeping model, and trajectory of a falling particle based upon the number of obstacles encountered: (b) one obstacle, (c) two obstacles, (d) three unstable obstacles, (e) three stable obstacles.

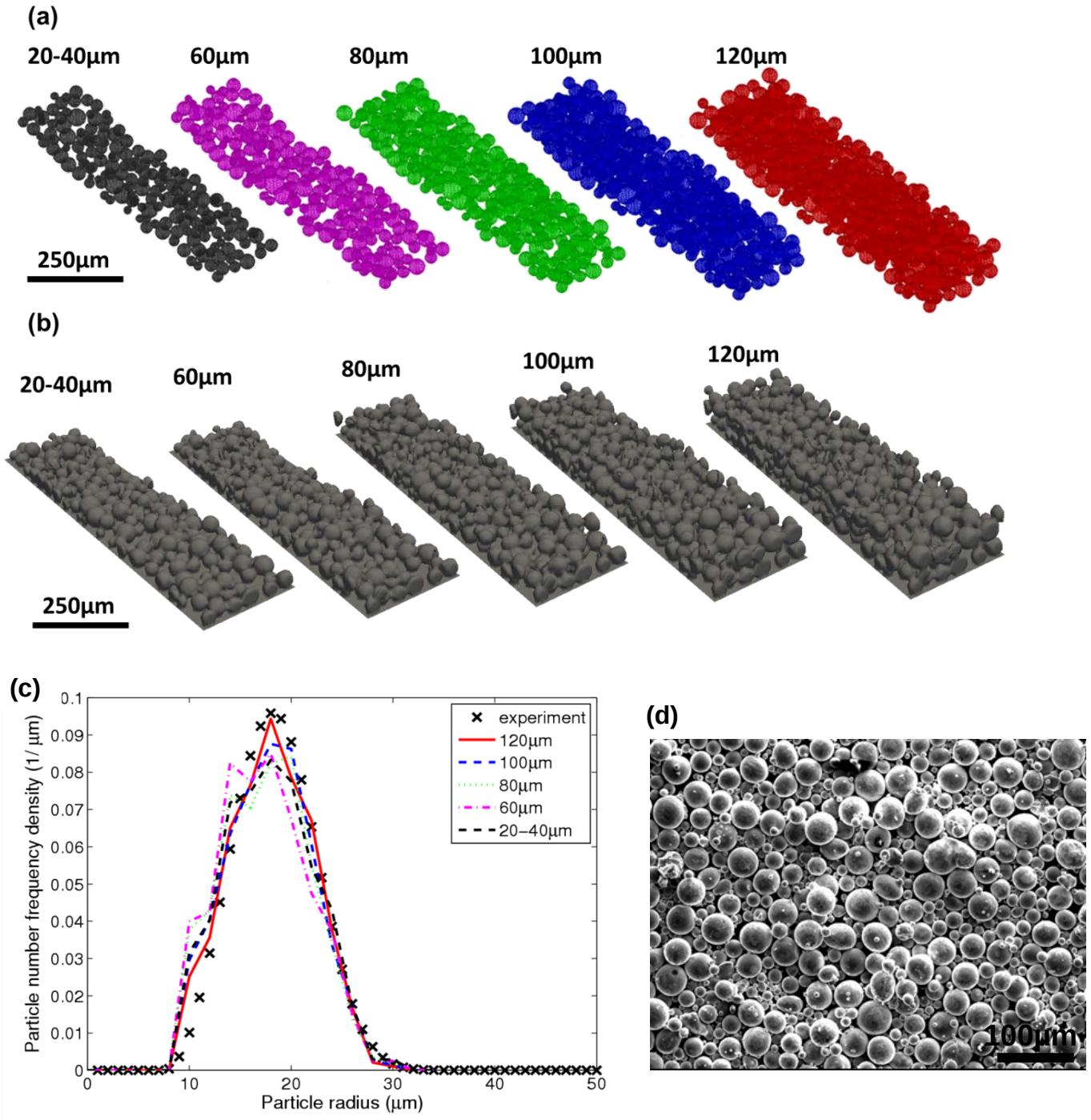

Figure 3: Simulated powder particle distribution in with different layer thicknesses: 20-40, 60, 80, 100, and 120µm using (a) powder dropping model and (b) replicated powder layer thickness used for the CFD calculation; (c) powder size distribution of Ti-6Al-4V measured using a laser diffraction particle size analyser, after [9], and generated powder distribution for 5 different powder layer thicknesses using particle dropping model developed from [16]; (d) SEM micrograph showing the actual particle distribution of as-received powder.

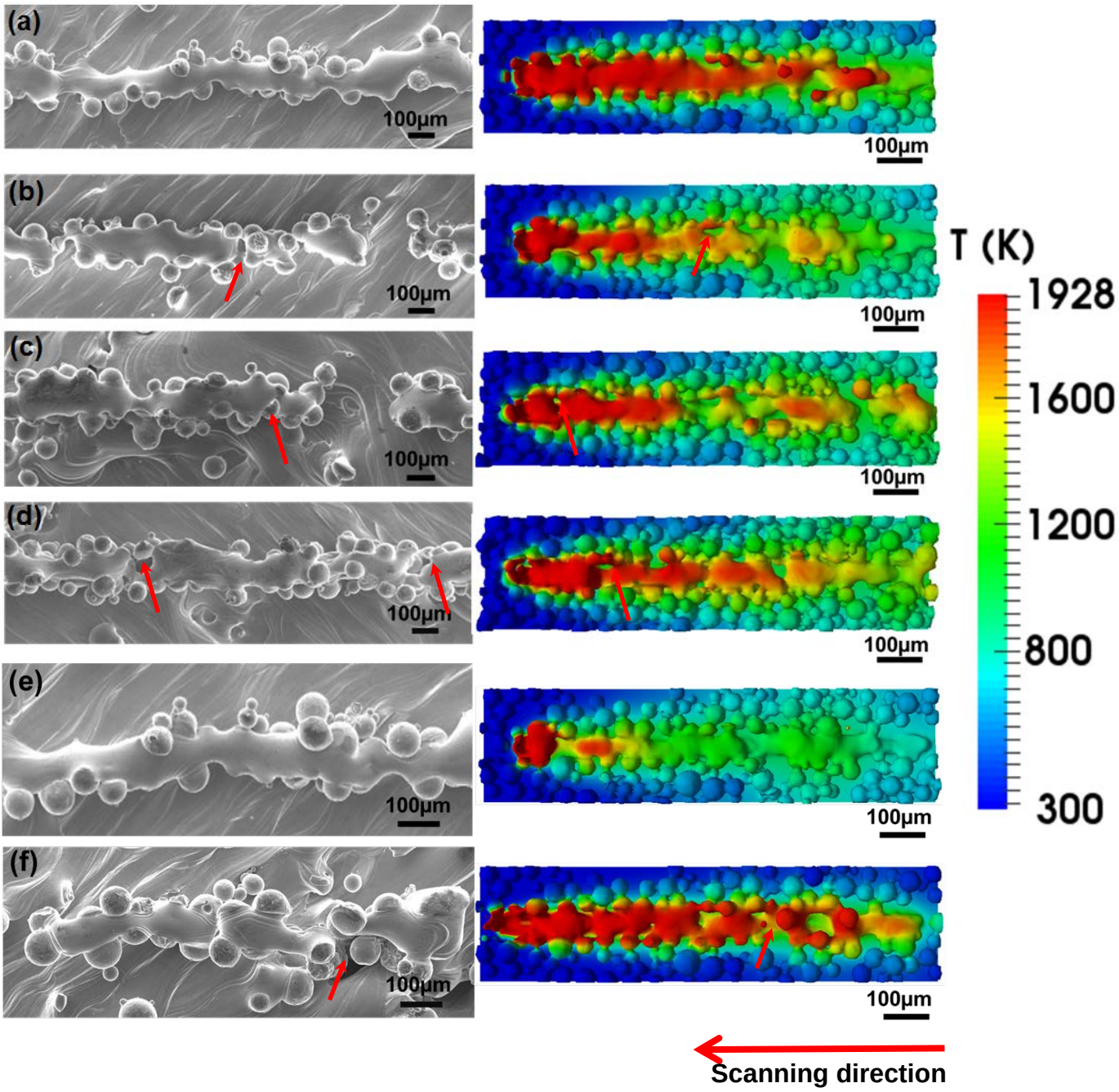

Figure 4: Surface morphology (left) measured on the top view of the single track scanning and (right) predicted from thermal fluid dynamics calculation for 4 different powder layer thicknesses: (a) 20 μm, (b) 60 μm, (c) 80 μm, (d) 100 μm, effect of (e) argon atmosphere and (f) fast laser scanning speed (4000mm/s) into the surface morphology, using 20μm powder layer thickness. The arrows point to the presence of cave-like pores.

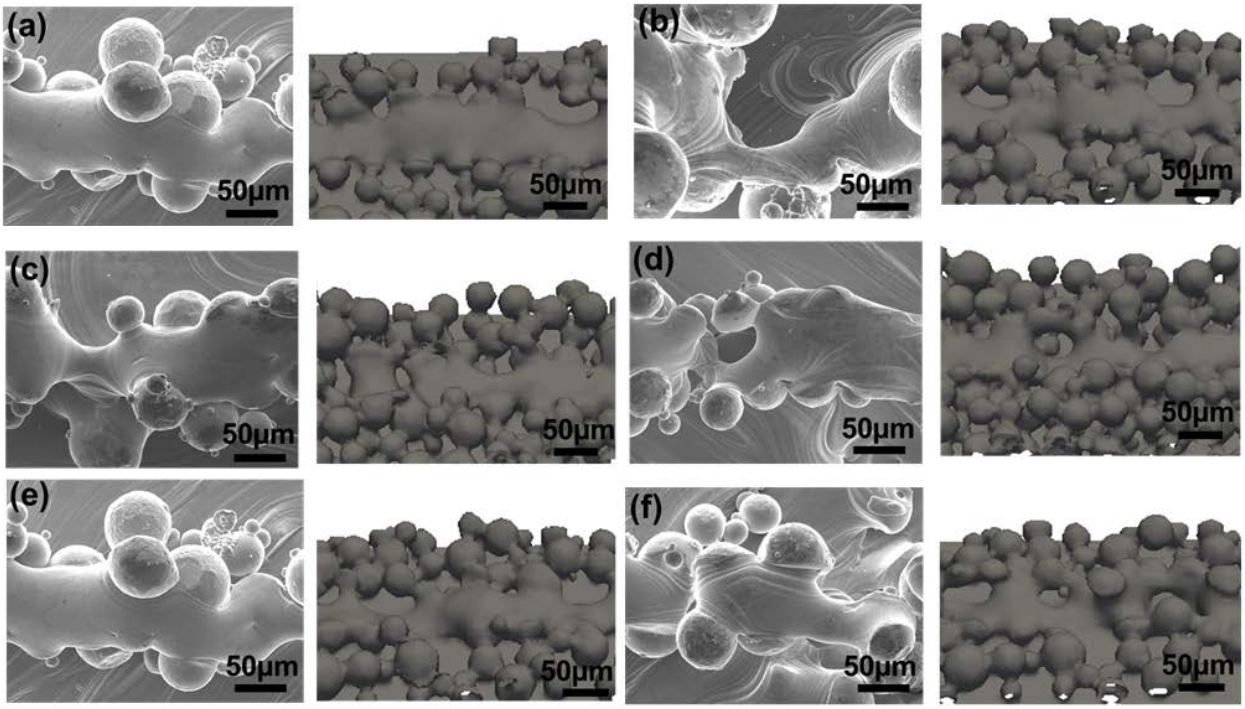

Figure 5: Magnification images of surface morphological structure after SLM scanning, compared between experiments (left) and CFD modelling (right), in various conditions [scanning speed, powder layer thickness, surrounding atmosphere]: (a) 2400mm/s, 20μm, air, (b) 2400mm/s, 60μm, air, (c) 2400mm/s, 80μm, air, (d) 2400mm/s, 100μm, air, (e) 2400mm/s, 20μm, argon, (f) 4000mm/s, 20μm, air.

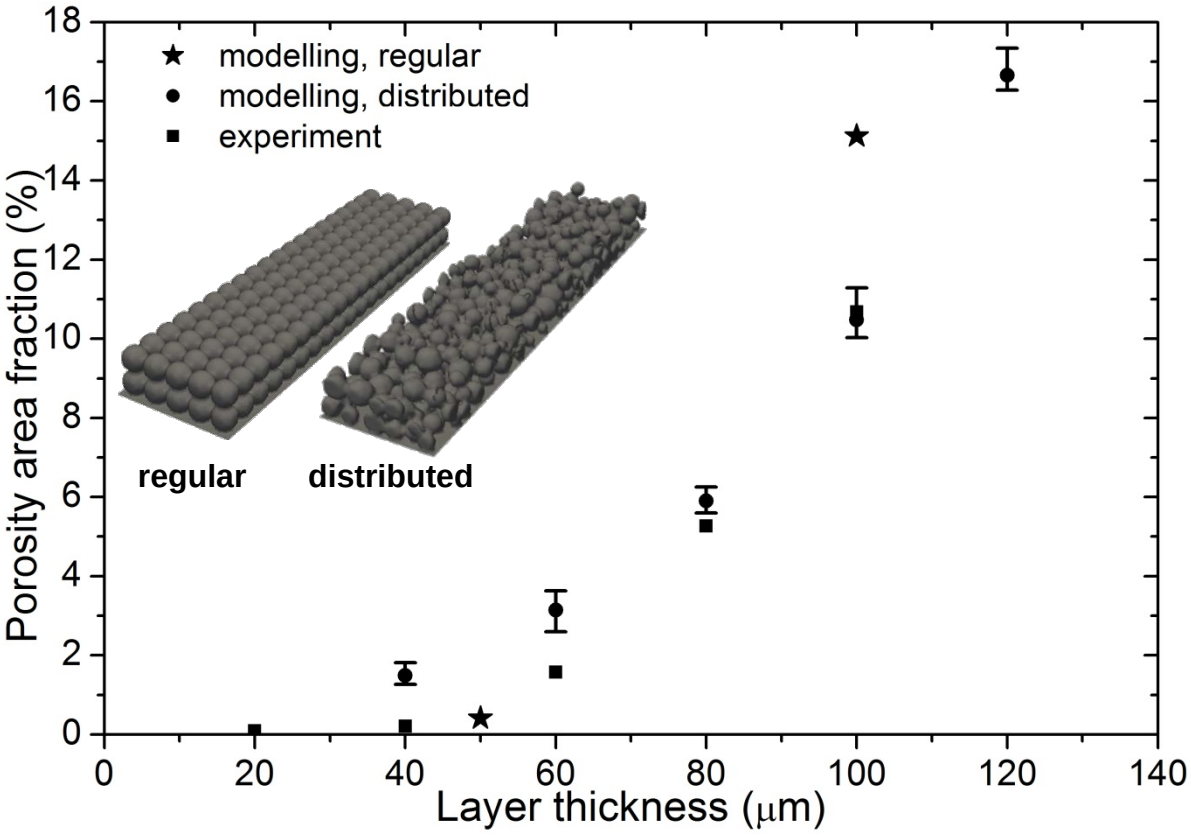

Figure 6: The comparison of porosity fraction using current modelling capability and available experimental data, varying the powder layer thickness.

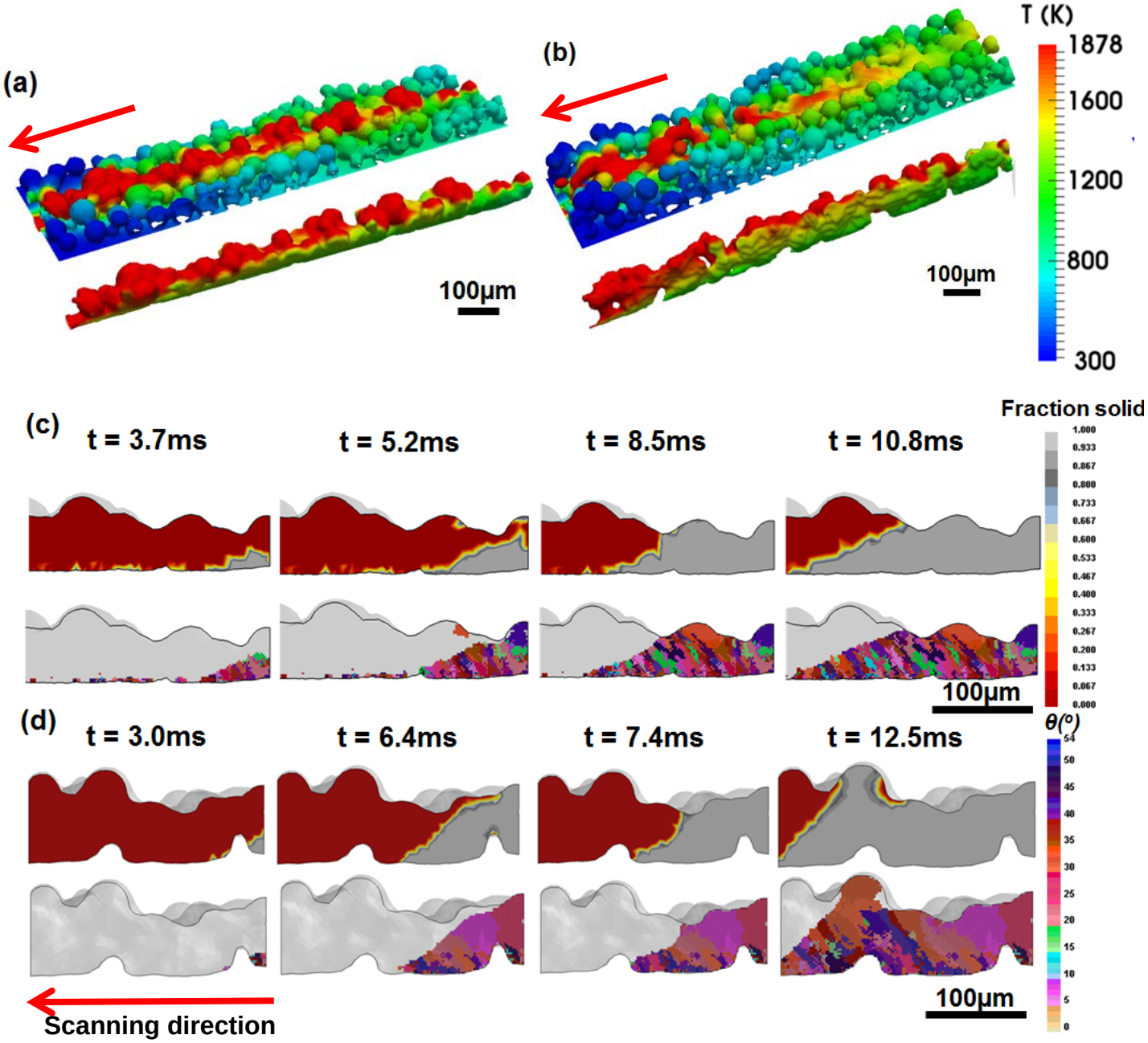

Figure 7: Linkage between thermal fluid dynamics calculation providing single track molten zone and dynamic nodal temperature history of (a) 20μm layer thickness, and (b) 100μm layer thickness, and cellular automata finite element calculations predicting SLM-processed induced grain microstructure evolution during the SLM-processed at (c) 20μm powder layer thickness and (d) 100μm powder layer thickness.

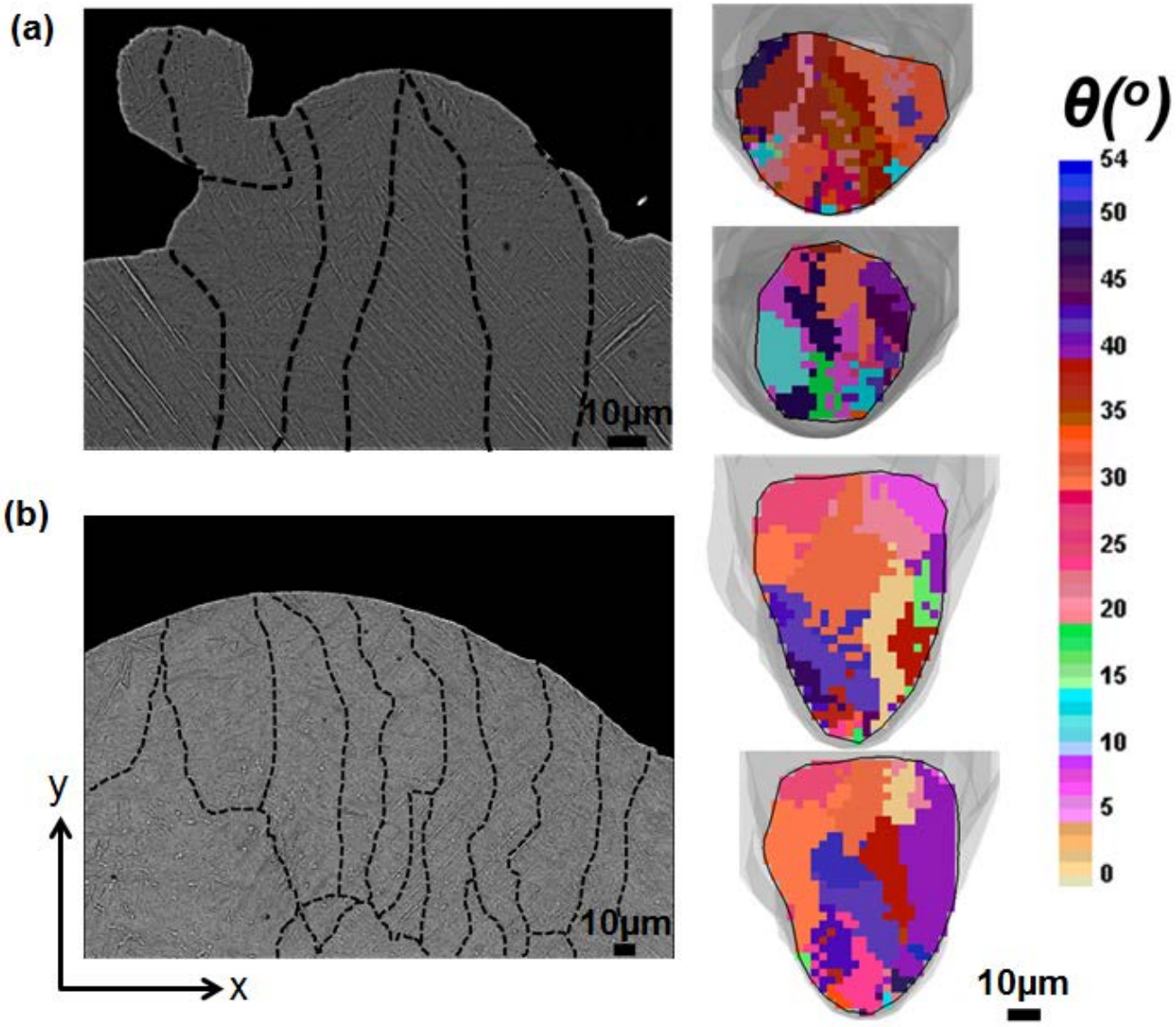

Figure 8: SEM micrographs show the grain morphology (left) and misorientation mapping within the single track (right) of: (a) 20μm powder layer thickness and (b) 100μm powder layer thickness.

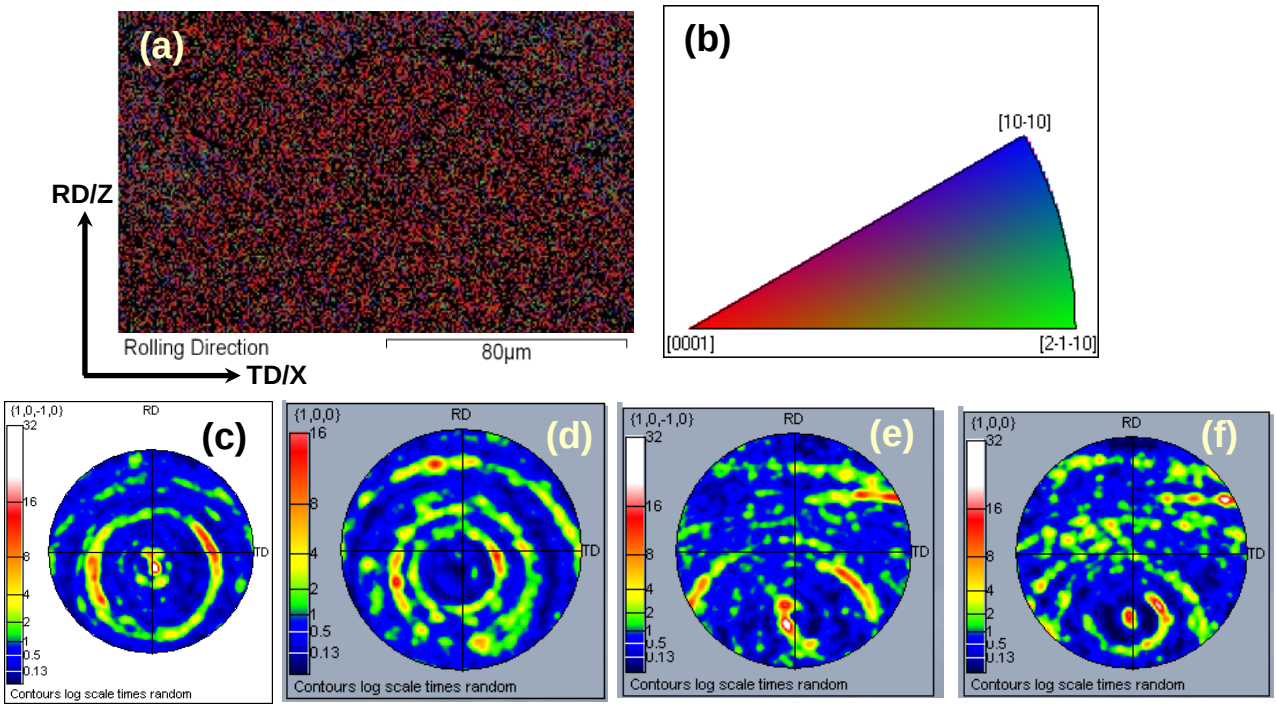

Figure 9: (a) EBSD image of the weld bead (shown in Figure 10(a)) fabricated at 2400mm/s and with a layer thickness of 20µm; (b) inverse pole figure for the sample shown in (a); (c) and (d) α′ and β pole figures for the sample shown in (a); (e) and (f) α′ and β pole figures for the weld bead (shown in Figure 10(b)) fabricated at 2400mm/s and with a layer thickness of 100µm

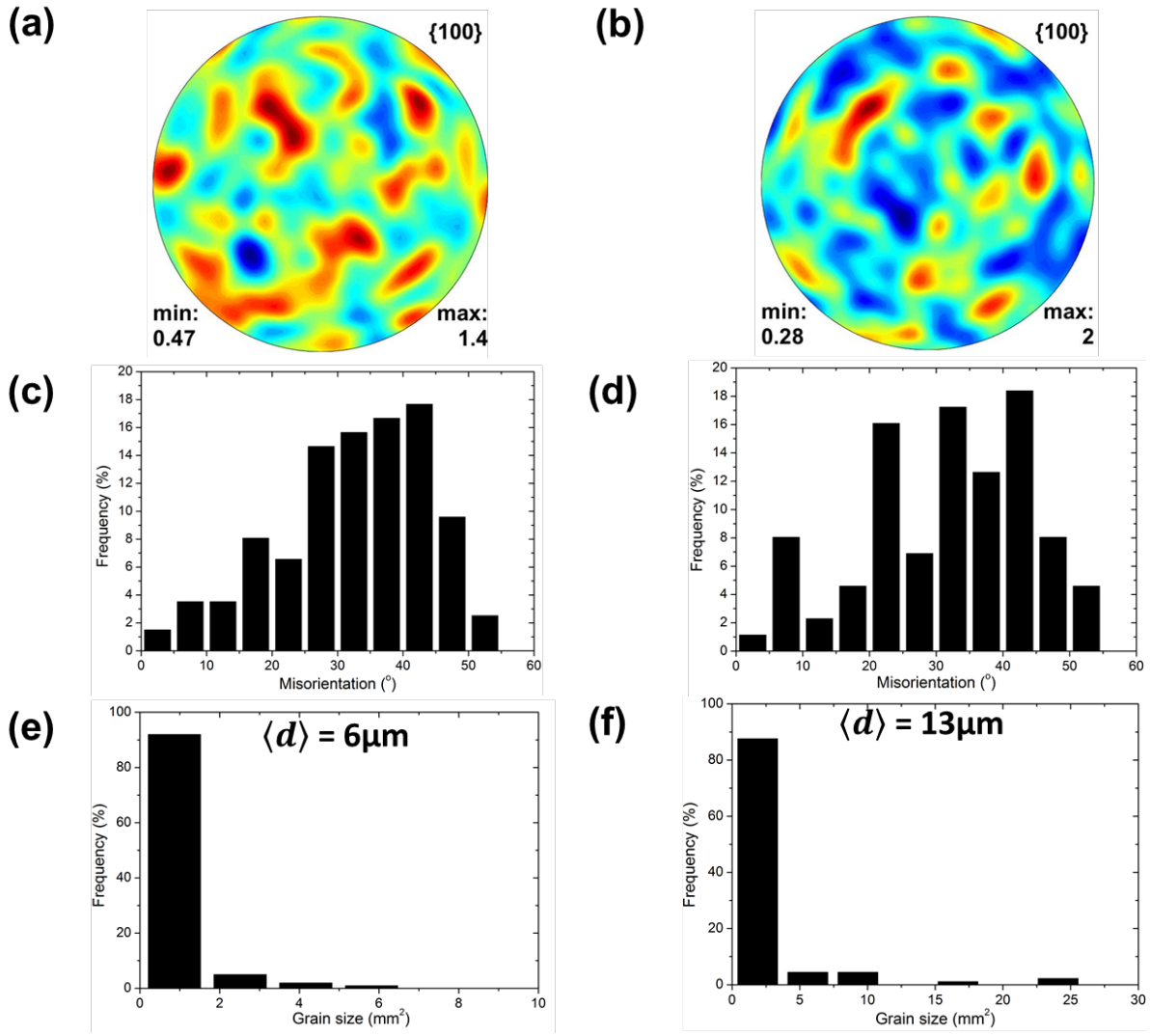

Figure 10: Predicted β-phase pole figures of (a) 20μm track and (b) 100μm track, misorientation maps of (c) 20μm track and (d) 100μm track, and grain size distribution of (e) 20μm track and (f) 100μm track.

Table 1: Data used for fluid flow and heat transfer calculations.

Physical properties	Ti-6Al-4V
Solidus temperature, (K)	1878
Liquidus temperature, (K)	1928
Evaporation temperature, (K)	3133
Density of liquid metal, ($kg.m^{-3}$)	4000
Molar mass, (g/mol)	446.07
Specific heat of solid metal, ($J\ kg^{-1}\ K^{-1}$)	670
Specific heat of liquid metal, ($J\ kg^{-1}\ K^{-1}$)	730
Thermal conductivity of solid metal, ($Wm^{-1}\ K^{-1}$)	21
Thermal conductivity of liquid metal, ($Wm^{-1}\ K^{-1}$)	29
Viscosity, (Pa.s)	0.005
Thermal expansion coefficient, (K^{-1})	8×10^{-6}
Surface tension, (Nm^{-1})	1.4
Temperature coefficient of surface tension, ($Nm^{-1}K^{-1}$)	-0.26×10^{-3}
Enthalpy of solid at melting point, ($J\ kg^{-1}$)	1.12×10^{6}
Enthalpy of liquid at melting point, ($J\ kg^{-1}$)	1.49×10^{6}
Enthalpy change of evaporation, ($J\ kg^{-1}$)	4.7×10^{6}
Atmospheric pressure, (Nm^{-2})	101300
Ideal gas constant, ($JK^{-1}\ mol^{-1}$)	8.314
Boltzmann's constant, ($J\ K^{-1}$)	1.38×10^{-24}

Table 2: Data used for heat source model in this calculation.

Heat source model parameters	Value
Power distribution factor	3.0
Total beam power, (W)	400
Effective absorption coefficient	0.24
Beam radius, (μm)	50
Beam velocity, (mm s^{-1})	2400 or 4000

Table 3: Data used for cellular automata finite element calculations in this work

Physical properties	Ti-6Al-4V
a_2, (m s^{-1} K^{-2})	1.06×10^{-7}
a_3, (m s^{-1} K^{-2})	1.03×10^{-6}
Gibbs-Thompson coefficient	2.00×10^{-7}